Journal of Power Sources

Modelling Electro-Chemical Induced Stresses in All-Solid-State Batteries: Anisotropy Effects in Cathodes and Cell Design Optimisation

Robert Mücke^a, Martin Finsterbusch^a, Payam Kaghazchi^a, Dina Fattakhova-Rohlfing^{a,b}, Olivier Guillon^a

^a Forschungszentrum Jülich GmbH, Institute of Energy and Climate Research, Materials Synthesis and Processing (IEK-1), 52425 Jülich, Germany; Jülich Aachen Research Alliance: JARA-Energy, 52425 Jülich

^b Faculty of Engineering and Center for Nanointegration Duisburg-Essen, Universität Duisburg-Essen, Lotharstr. 1, 47057 Duisburg, Germany.

Keywords: all-solid-state batteries, stress state during delithiation, isotropic and anisotropic properties, crystallographic orientation, cell design

Abstract

All-solid-state lithium batteries offer promising advantages in energy density and safety compared to conventional lithium ion batteries. However, the majority of this type of batteries suffers from a low cycling stability, which might originate from mechanical fatigue caused by mechanical stresses and strains in the rigid structure. We introduce a general approach to model and analyse the stresses in rigid cathode/electrolyte electrodes on a cell level, which enables to develop optimised cell designs with an improved mechanical stability. We apply this approach on composite cathodes with a Li₇La₃Zr₂O₁₂ (LLZO) ceramic electrolyte and LiCoO₂ (LCO) active material. Using the 3D microstructure of a real cathode, the stresses inside a free-standing electrode and model cells with a thin and a thick LLZO separator are calculated for the charging cycle considering isotropic and anisotropic material properties of LCO as well as non-textured and textured crystallographic alignment. Compared to randomly oriented crystals, the textured crystallographic alignment of LCO grains, introduced by the manufacturing process, has a significant effect and yields considerably better stress distributions in all cell configurations investigated. The design of optimised allsolid-state cells with reduced separator thickness leads to a significantly more favourable stress state than a typical lab scale separator-supported cell.

1. Introduction

All-solid-state lithium batteries have attracted increasing attention over the past years due to their promising advantages in energy density, stability and safety over conventional lithium ion batteries. [1] Within the two major classes of ceramic electrolyte materials (sulphides and oxides), the thio-phosphates (e.g. LSPS [2] and LGPS [3,4]) show the highest conductivity and are easy to process into battery cells due to their ductility. Even so, thio-phosphates suffer from a narrow window of electrochemical activity. Further, still a rather high mechanical pressure needs to be applied to most sulphide based all-solid-state batteries during operation, even though very recent improvements were made to this regard. [5] In contrast, oxide based ceramic solid electrolytes such as the garnet type $\text{Li}_7\text{La}_3\text{Zr}_2\text{O}_{12}$ (LLZO) and its derivatives show better electrochemical stability against various cathode active materials [6,7] and is until now the only ceramic electrolyte (electro-)chemically stable against Li-metal anodes. [8] Due to the

necessary high temperature sintering step, good interfacial contact is ensured and such cells do not require external pressure during operation. However, this comes with the drawback that the interface is very rigid and cannot accommodate volume changes when all-solid-state cathodes composed of a mixture of active and ionic conductive material are operated.[9,10]

To achieve high energy densities, layered oxides of the quasi ternary phase diagram LiCoO₂, LiNiO₂ and LiMnO₂ are the typical active cathode materials of choice, due to their tuneable power capability, capacity and safety. However, all layered oxides suffer from cycling degradation, with the most possible mechanisms being transition metal leaching and crystal structural changes accompanied by non-negligible volume changes. [11-20] For example, Li_xCoO_2 undergoes monoclinic transition at x < 0.5.[21] Hence in practice, LCO cathodes are delithiated only to Li_{0.5}CoO₂ which causes a positive volume expansion of 2%.[22,23] Furthermore, layered oxides exhibit strong anisotropic material properties, both with respect to Li ion conductivities and electro-chemo-mechanical behaviour during cycling. For liquid based Li-ion batteries, these anisotropy effects on the degradation were investigated on single grain level using model microstructures.[11,17] For all-solid-state batteries, degradation due to volume changes of the active material is different as all materials involved are rigid, the electrolyte of composite cathodes interacts mechanically with the active material, and the separator is mechanically connected which can lead to very different stress distributions. That ceramic electrodes degrade mechanically is well known [18-20] and the derivation of the physical model for the anisotropic stress calculation is straight forward as formulated in Roberts et al. [24]. However, stress calculations have so far only been carried out for cathodes in liquid electrolytes. This may be due to the fact that it is rather difficult to acquire a 3D microstructure of multiple phases in the required quality as well as the numerical discretisation at high resolution.

For layered oxide active cathode materials in liquid electrolytes, stresses have been calculated on the particle level using isotropic [25-27], partly anisotropic [17] and full anisotropic [28] material parameters mostly considering the discharge kinetics. As a step towards the analysis of complex microstructures, the stresses originating from differently aligned primary particles of active cathode materials coupled together in secondary particles have been calculated for model and realistic 2D microstructures.[24,29-31] We recently reported on a significant improvement of the stress state when textured microstructures are used in secondary particles of active material in lithium ion batteries with liquid electrolytes.[31] Finally, the stresses inside larger 2D and reconstructed 3D microstructures of active cathode materials have been studied using isotropic material properties during discharge.[32-35] One of the very rare publications on stresses in all-solid-state batteries connects induced pressure changes to changes in open-circuit voltage using model cells based on sulphide electrolytes.[23]

In this work, we investigate the strains and stresses induced in the mixed LLZO/LCO cathode of a sintered all-solid-state battery using its reconstructed microstructure as input parameter for continuum modelling. For the calculation of stresses and strains in these complex structures, a grid based mechanical solver was used which circumvents the generation of complex finite element meshes. The results of the complex stress states were quantified and visualised comprehensibly in material selective histograms using the maximum principle and shear stresses. Since LCO exhibits a pronounced anisotropic expansion behaviour [22] and the layer manufacturing process can introduce significant texturing of the microstructure, the effect of texture was investigated and contrasted to randomly orientated grains. The

anisotropic material properties of LCO were taken into account [24] and the results were compared with those obtained from isotropic calculations. Additionally, we studied the mechanical stability of optimised all-solid-state cells with reduced separator thickness. Many previous works calculated the stresses during the lithiation of the cathode, i.e. during the discharge of the cell, and assume the charged state to be stress-free beforehand.[25,26,28,32-35] However, the electro-chemically stresses are introduced during the first change of the degree of lithiation. Therefore, we select the as-manufactured fully lithiated cathode as starting point.[29-31] No significant stresses are present during the sintering process of manufacturing and the thermal stresses are smaller than the electro-chemically induced stresses as the strain differences of the chemical expansion are at least twice as large as the strain differences of the thermal expansion ($\Delta T=1000 \text{ K}$).[22,36,37] Hence, in this work, the delithiation (charging) cycle is investigated and material properties of Li_{0.5}CoO₂ are used which significantly differ from the properties of fully lithiated LiCoO₂.[29]

Elucidating and understanding the mechanisms of mechanical fatigue of mixed cathodes and full cells based on solid-state electrolytes and layered oxide cathode active materials is crucial to develop design guidelines and failure mitigation strategies. These investigations are indispensable to enhance all-solid-state batteries towards industrial feasibility.

2. Experimental and Simulation Methods

2.1 Sample preparation

The mixed cathode was prepared using a 2:1 mass ratio of LCO (MTI Corp., Richmond, CA, USA) and Li_{6.6}La₃Zr_{1.6}Ta_{0.4}O₁₂ (LLZO:Ta; prepared at IEK-1) powder. An ink was prepared with 6 % ethyl cellulose (Sigma-Aldrich, Darmstadt, Germany) dissolved in terpineol (Sigma-Aldrich), a thinner (type 8250, DuPont, Neu-Isenburg, Germany) and the ceramic powder in a weight ratio of 3:2:5. The ink was painted on small LLZO:Ta disks and sintered at 1050 °C for 30 minutes. The thickness of the mixed cathode is typically in the range of 20-50 μ m and the details on the fabrication process and subsequent electrochemical performance of the cells can be found in our previous reports.[9,10]

A composite specimen with 1:1 weight ratio of LCO:LLZO was manufactured for the electron backscatter diffraction (EBSD) analysis.

2.2 3D reconstruction of the microstructure using FIB-SEM

An image stack of cross sections was acquired by focused ion beam SEM. The surface of the samples was coated with a 1 μ m platinum layer to ensure sufficient electrical conductivity. The FIB sections were produced with a dual beam FIB Helios 600i (FEI, Hillsboro, USA) using Ga⁺ ions. First a 42×30×50 μ m³ base was cropped and then slices with a thickness of 50 nm were cut with an ionic current of 2.5 nA. Back scattering electron images were obtained under an angle of 52° towards the sectioning plane. The horizontal resolution was 50 nm; the images were processed to yield an isotropic voxel size of 50 nm. The following steps were carried out for the 3D reconstruction: (1) Adjustment to uniform brightness of the image stack, (2) moving frame cropping to compensate tilt image shift (with a self-written Matlab script), (3) image alignment to smoothen out vibrations perpendicular to the stacking axis (using a Matlab script based on the Lucas-Kanade image alignment algorithm[38]), (4) denoise filtering to enhance threshold binarisation (ImageJ anisotropic diffusion filter [39]), (5) advanced binarisation (with a self-written Photoshop script). Special care was needed for the binarisation of the three phases to avoid artefacts: The intermediate grey tones between

the bright LLZO and dark pore phase should not be identified as LCO which also appears as middle grey. Smaller pores inside LLZO also exhibited the grey value of LCO, but were to be identified as pores. Larger pores that contain the shades of material located more inside the sample due to the depth of field were to be identified as clear black pores. Sample specific size filters using the masking tool in Photoshop were used to handle these issues. An example of a resulting image is shown in Fig. S1 (compare Fig. 3a,b).

2.3 Material parameters for the simulation

The calculations have been carried out for an isotropic case (isotropic volume change and isotropic material properties) and two anisotropic cases: randomly aligned and parallel aligned LCO crystals. Randomly oriented LCO crystals reflect a realistic instance for a macroscopically isotropic behaviour as the anisotropic nature of the LCO crystals themselves is always present. For the parallel aligned LCO crystals, the *c* axis of the crystal was assumed to be perpendicular to the coating plane which was confirmed by an EBSD analysis of a sintered cathode layer.

During 50% delithiation, LiCoO₂ shrinks very slightly along the a and b axis of its hexagonal lattice by -0.23% (Tab. 1). However, due to its layered atomic structure and the pronounced electrostatic repulsion of oxygen in adjacent layers during the removal of Li⁺, it expands significantly along the c axis (+2.39%). This corresponds to a volume change of +1.91% which is in agreement with the data of Reimers and Dahn[22] who found +1.86%. For the isotropic calculations an effective strain of 0.63% was used in this work. The charging rate was assumed to be slow enough so that Li concentration gradients inside Li_xCoO₂ were negligible. As we study the boundary conditions of mere delithiation in this work, no thermal mismatch stresses of the manufacturing processes were taken into account.

Tab. 1: a) Anisotropic crystallographic strains of LiCoO₂ during delithiation (hexagonal lattice) based on X ray diffraction of single crystals.[40,41]

	a axis	c axis
LiCoO ₂ [40]	2.8155 Å	14.0537 Å
Li _{0.5} CoO ₂ [41]	2.809 Å	14.389 Å
change	-0.23%	2.39%

The mechanical properties of fully lithiated $LiCoO_2$ have been assessed experimentally with different techniques: Pulse echo measurements yielded a Young's modulus of $E = 191\pm10$ GPa and a Poisson ratio $\nu = 0.24$ [36] whereas nano-indentation resulted in $E = 174\pm25$ GPa.[42] For (partly) delithiated LCO no experimental values have been reported so far. Theoretical DFT calculations from Yamakawa *et al.* [29] yielded a stiffness matrix of

$$\mathbf{C} = \begin{pmatrix} 303.86 & 101.71 & 32.58 & 0 & 7.31 & 0 \\ 101.71 & 318.93 & 28.66 & 0 & -3.93 & 0 \\ 32.58 & 28.66 & 98.93 & 0 & 7.03 & 0 \\ 0 & 0 & 0 & 18.02 & 0 & -2.46 \\ 7.31 & -3.93 & 7.03 & 0 & 15.73 & 0 \\ 0 & 0 & 0 & -2.46 & 0 & 101.94 \end{pmatrix}$$
GPa (1)

for Li_{0.5}CoO₂ which is used in this work. It is close to the stiffness matrix underlying the results of Wu *et al.*[43] According to the Voigt-Reuss-Hill approximation for isotropic polycrystals,[44] it corresponds to a Young's modulus of $E_{\text{L0.5CO}}$ =123.6 GPa and a Poisson ratio of $v_{\text{L0.5CO}}$ = 0.288 which were used in our isotropic calculations. For fully lithiated LiCoO₂, the DFT calculations of Yamakawa *et al.* [29] yield a Young's modulus of E = 210 GPa and a Poisson ratio of v = 0.26 which are close to the abovementioned experimental values.

As LLZO exhibits a cubic crystallographic structure, no anisotropic behaviour is expected. The Young's modulus of the Al doped LLZO we used has been determined by nano-indentation to be $E_{\rm LLZ} = 146$ GPa.[45] The experimental value of $\nu_{\rm LLZO} = 0.26$ was applied for its Poisson ratio.[46,47] Since the Li content in LLZO does not change during charging and discharging, it is not subjected to any volume change.

2.4 Simulation setup and boundary conditions

Three different model cell configurations with appropriate boundary conditions were used (Fig. 1):

- (a) The 3D microstructure acquired by FIB-SEM with the final dimensions of $26.5 \times 16.5 \times 16.5 \times 16.5 \, \mu m$ (530 \times 330 \times 330 voxels) served as representative volume element (RVE) of a bulk cathode of infinitive extent using symmetric (Dirichlet) boundary conditions in all directions without any constrains.
- (b) The same microstructure was mirrored forming a $50 \times 50 \times 50$ µm cathode structure on top of a thick separator to model a separator-supported design. The microstructure was down-sampled to a voxel size of 100 nm to reduce computational costs (no difference in the stress histograms was observed comparing the original bulk RVE with a voxel size of 50 nm and the down-sampled bulk RVE with a voxel size of 100 nm). The 400 µm thick LLZO separator was implemented as a 50 µm layer with an 8 times increased stiffness (1168 GPa) to keep the geometry in practicable size. The stress values occurring inside the separator were divided by a factor of 8 to represent again the original physical configuration. No bending was allowed as the battery housing would normally constrain any bending. The horizontal surfaces were treated as free surfaces whereas the lateral faces were again modelled with symmetric boundary conditions to represent a continuous layer. The total domain size was $500 \times 500 \times 1000$ voxels.
- (c) For the cathode-supported design a 100 μ m thick cathode was attached to a thin separator with a thickness of 4 μ m. The conditions were the same as for the separator-supported design except that no stiffness scaling was required for the separator. The model size of this configuration was $50 \times 50 \times 104 \ \mu$ m ($500 \times 500 \times 1040 \ voxels$).

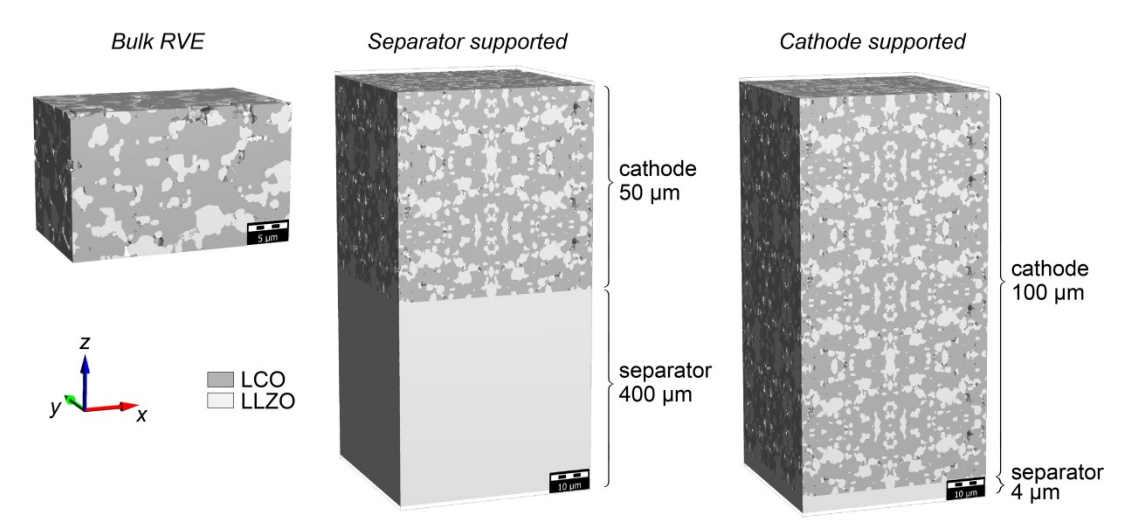


Fig. 1: The different investigated cathode configurations: a) free-standing cathode (as acquired by FIB-SEM), b) 50 μ m cathode supported by a thick separator, c) thick 100 μ m cathode acting as mechanical support for a thin separator.

For the random anisotropic case, the microstructure of the LCO was segmented into grains using the watershed method (GrainFind module of GeoDict, Math2Market GmbH, Kaiserslautern, Germany) yielding a modal volume weighted diameter of 2.7 μ m. Each grain was assigned a random set of Euler angles (φ , θ , ψ) resulting in a uniform distribution of orientations.

All stress calculations were carried out using the ElastoDict FeelMath-LD module of the GeoDict software with a conjugate gradient voxel based solver. As the geometry was discretised with a regular voxel grid, there was no need to perform a complex meshing required by typical finite element solvers. All deformations were very small, therefore, the small deformation theory was employed.

2.5 Stress representation

The principal stress with the maximum average absolute value, S_{max} , was calculated from the mean principal stresses σ_i (i=1...3) for each material: $S_{\text{max}} = \sigma_j$ with j: $|\sigma_j| = \max_i |\sigma_i|$.

For the stress histograms, the differential relative frequency \tilde{n}_k was determined from the absolute frequency N_k of the stress S inside the stress interval $[S_k, S_{k+1}]$ by:

$$\tilde{n}_k = \frac{N_k}{(S_{k+1} - S_k) \sum_j N_j}$$

which is independent from the interval size chosen. In this work, an interval size of $S_{k+1} - S_k = 8$ MPa was used.

3. Results and Discussion

The LCO grains of the raw powder exhibited a clearly layered morphology (Fig 2a) which lead due to the anisotropic shape after powder processing to a strongly textured alignment in the applied layer (Fig 2b). As indicated by the electron backscatter diffraction (EBSD) results in Fig 2c, the crystallographic c axis of the LCO (which is perpendicular to the visible grain layers in Fig 2a) is mainly aligned parallel to the macroscopic z axis.

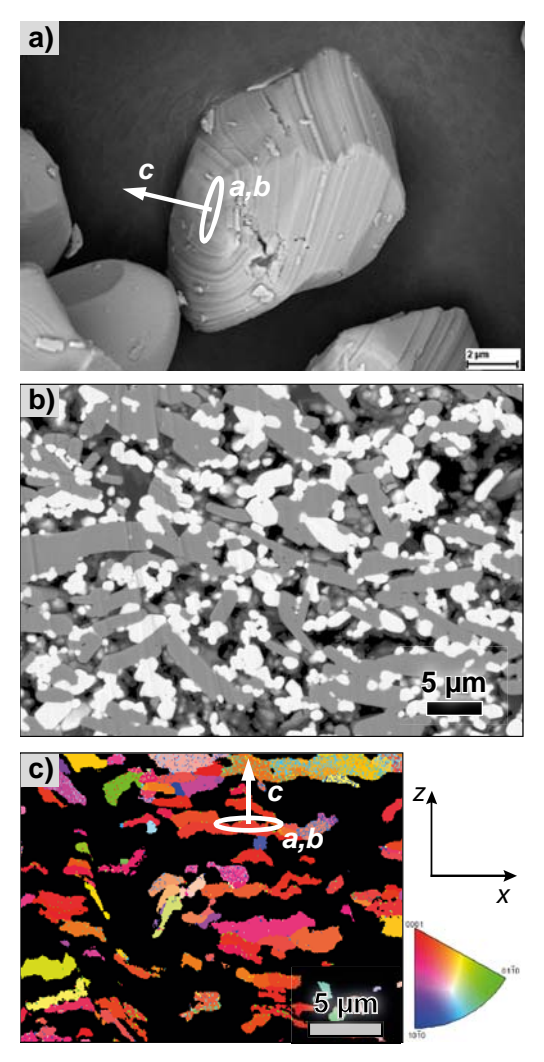


Fig. 2: a) Layered morphology of raw LCO powder acquired by SEM, b) SEM cross section of a sintered LCO/LLZO composite cathode and c) EBSD analysis of the same sample showing a strong preferential horizontal orientation of the crystals (the crystallographic c axis is parallel to the z which is normal to the coating's plane).

The volume fractions of the reconstructed bulk RVE were 64% for LCO, 26% for LLZO and 10% pores (Fig. 3 a,b). When LCO expands during delithiation, it is constrained by the neighbouring LLZO framework of the composite cathode. For a free-standing mixed cathode, this will introduce (negative) compressive stresses in the LCO and counteracting (positive) tensile stresses in the LLZO phase. For the isotropic case, the normal stresses along the different directions are on average equal to –170 MPa for the LCO and 470 MPa for the LLZO (Fig. 3 d,g; Fig S2 a). Although the Young's moduli of LCO and LLZO are comparable in the delithiated state, the volume fraction of LCO was considerably larger than the fraction of LLZO in the composite, thus, the less abundant LLZO suffers larger absolute stress values to maintain the equilibrium of forces. The average stress profiles (Fig. S2 a) for the different stress and profile directions do not exhibit any significant differences. Hence, the texture of the microstructure inside the layer did not introduce any stress anisotropy when the crystallographic orientation remains unconsidered. In order words, it is not the textured microstructure itself that introduces the later seen stress anisotropy, but solely the anisotropic material behaviour along the different crystallographic axes.

The two anisotropic cases considered in the following (randomly oriented and parallel textured) have both their practical relevance: The random anisotropic alignment occurs when perfectly spherical particles are used that will not show any specific crystallographic orientation after layer preparation whereas the parallel texture will be prevalent for flake-like particles that become aligned during wet-chemical manufacturing processes such as roll-coating, screen printing, or tape casting.

When the macroscopic isotropy is more realistically represented by randomly oriented anisotropic grains instead of isotropic particles, the normal stresses inside the individual grains increase (Fig. 3 e,h) as adjacent LCO grains can now induce stresses in one another due to their different expansion in a given macroscopic direction. This can even lead to a stress inversion: tensile stresses in LCO and compressive stress in LLZO grains. The overall mean values of the normal stresses remain similar (Fig S2 b) since the contribution of the grain orientation levels out; apart from fluctuations on the grain level, no stress gradients were observed in the RVE. On the other hand, there is a significant increase in the normal shear stresses components for the random anisotropic case (Fig. S3) which affects the principal stresses discussed later.

For the parallel aligned anisotropic LCO, the prevalent crystallographic orientation in the x-y plane result in almost negligible small strains and stresses in the x and y direction (Fig. 3 f; S2 c; S4 c) whereas almost all volume change takes place in the out-of-plane (z) direction yielding significant values of the normal stresses component σ_{zz} (Fig. 3 i, S4 f). This is in agreement with the observed sheet-wise disintegration of LCO particles perpendicular to the same direction.[48] This effect would be even larger if it was not reduced by the small stiffness in the c (= z) direction (\mathbf{C}_{33} in equ. 1). Again, the stresses are constant over the bulk volume element disregarding grain level fluctuations (Fig. S2c).

For brittle materials, the value of the largest principal stress is of most importance in failure analysis, e.g. according to the Rankine criterion. Considering the principle stresses with the maximum absolute value, S_{max} , the random anisotropic case yields the extremely high stresses of -1170 ± 380 MPa for the main stress regimes in LCO and 1110 ± 510 MPa in LLZO and a large fraction of grains under stress inversion (Fig 3k and Fig. 4b). An ideal isotropic calculation leads to a significantly smaller and narrower distribution without any stress inversed grains (Fig 3j and Fig. 4a). The principal stresses are reduced when the LCO crystals are aligned in parallel (-470 ± 260 MPa for LCO and 1060 ± 540 MPa for LLZO) as well as the volume fraction under stress inversion (Fig 3l and Fig. 4c). The lower stresses in the parallel aligned case are accompanied by larger total strains (Fig. S4); nonetheless, as they mainly appear in the z axis they are not detrimental in a constrained configuration with a separator shown in the following.

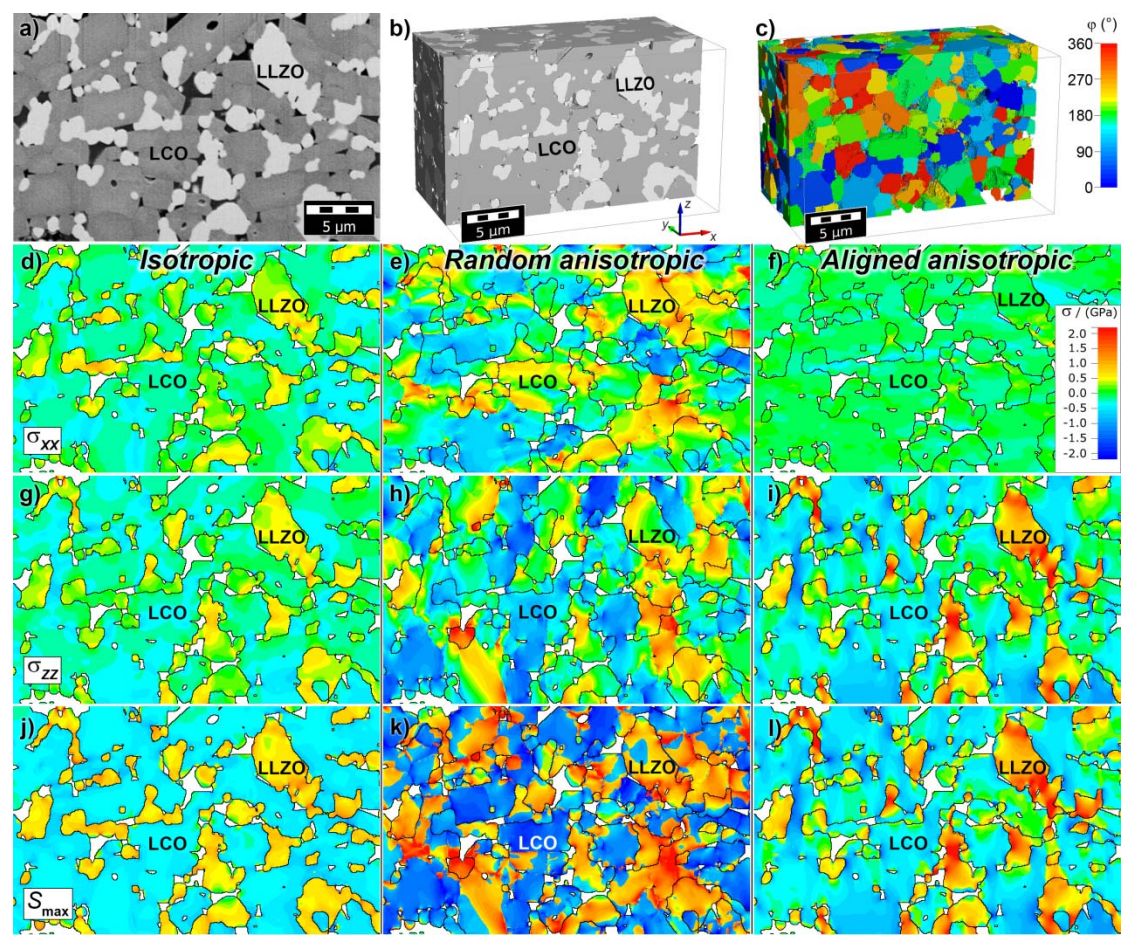


Fig. 3: Stress distribution inside a free-standing mixed LLZO/LCO cathode (bulk RVE). a) original SEM cross section, b) corresponding slice of the total reconstructed RVE, c) distribution of the Euler angle φ of the randomly oriented LCO grains after segmentation., d)-f) normal stress in x direction, g)-i) in z direction, j)-l) principal stress with maximum absolute value; for isotropic (d, g, j) and anisotropic LCO material properties with randomly aligned grains (e, h, k) and parallel aligned grains (c axis ||z| axis; f, i, l). The colour code for the stress contours was kept constant.

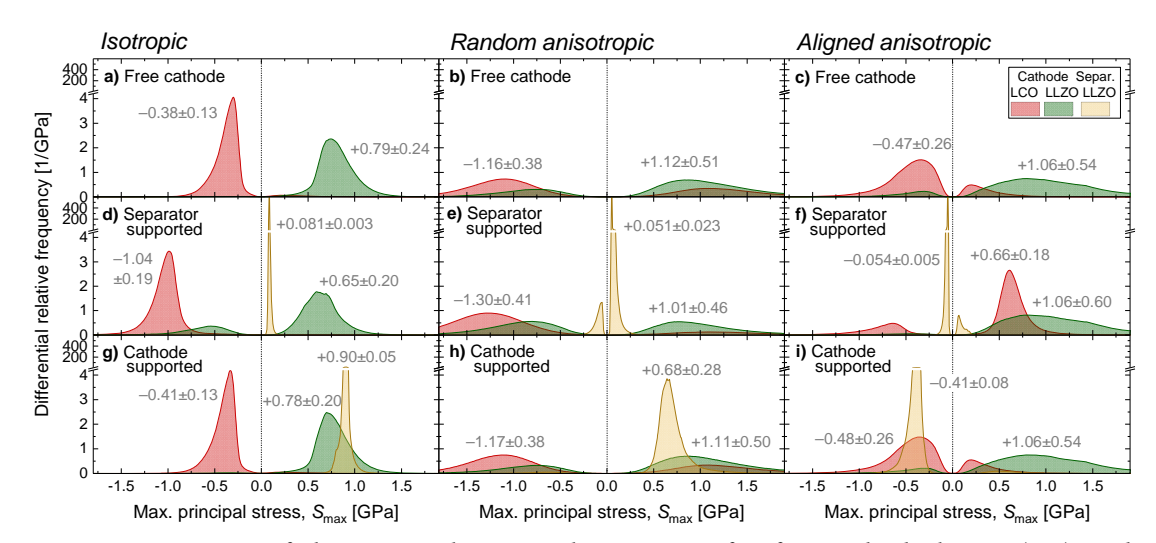


Fig. 4: Histograms of the maximal principal stress S_{max} for free cathode layers (a-c) and constrained cathode layers in a separator-supported (e-f) and cathode-supported cell design

(g-i). a,d,g) isotropic material properties of LCO, b,e,h) considering anisotropic material properties with random crystallographic orientation, and c,f,i) with parallel crystallographic alignment. The arithmetic mean values and the standard deviation of the main peaks of the distributions are given in GPa.

Advancing to a separator-supported configuration, the stress distributions of the LCO change signficantly (Fig. 4 d-f): Whereas for the ideal isotropic case large compressive stresses up-to 1.5 GPa occurred that raise beyond 1.5 GPa for the random anisotropic case, the parallel anisotropic alignment leads to tensile stresses around 660 MPa. This illustrates how important the consideration of the anisotropic properties of LCO and its orientation is in stress calculations. This is also emphasised by stresses inside the LLZO separator in the cathode-supported design: The isotropic and random anisotropic cases forecast large detrimental tensile stresses for the separator whereas the stresses are compressive and more moderate considering the aligned anisotropic configuration.

The ultimate compressive strength for fully lithiated LCO was measured by Feng *et al.*[49] to be 5.6 GPa for its pristine state which strongly decreased during electrochemical cycling presumably due to formation of Li⁺ vacancies or intercalated H⁺ (4 and 2 GPa after 1 and 11 cycles). For the delithiated state Wu and Zhang [43] obtained by DFT calculations that LCO loses approx. 20% of its strength during delithiation to Li_{0.5}CoO₂. There is no such data available for LLZO, neither for compressive nor tensile test configurations. Typical bending or ring-on-ring tests yield macroscopic stress levels that cannot be compared with the microstructure-resolved data of a grain level simulation as the first do not reflect the internal stress intensification due to presence of pores or grains geometries and consider a mixed compressive and tensile load case. The resulting experimental values are thus rather small (approx. 55 MPa by ring-on-ring [50], 160-240 MPa by bending test depending on the processing, grain size, and density of the samples [51]).

The stresses inside the mixed cathode are constant on a larger scale throughout the layer except at the free surface (Fig. S5): here, the out-of-plane component (σ_{zz}) decreases to zero and, due to the transverse deformation of the deeper material, a stress inversion occurs in the in-plane components (σ_{xx_0} , σ_{yy}) at the surface.

Considering the principal stresses for the aligned anisotropic orientation, it is deduced that:

- (1) The LLZO in the electrode suffers siginificant tensile stresses in all configurations which may lead to mechanical fatigue and ionic isolation of part of the active storage material. The relative ionic conductivity of the reconstructed composite microstructure was calculated to be only 3% compared to a bulk LLZO layer of same size. The ionic conductivity of LLZO is already a limiting factor in the performance compared to the higher electronic conductivity of LCO. Therefore, the stress-initiated fatigue of LLZO is seen as a dominating factor of the decreasing cell performance.
- (2) The LCO suffers significant tensile stresses of around 600 MPa in the separator-supported design which is considered as critical concerning its integrity. On the other hand, the compressive stresses of LCO in the cathode-supported cell configuration are below the compressive ultimate strength of LCO and thus more tolerable. The compressive stresses LLZO of the separator in the cathode-supported cell configuration of around 400 MPa are still in the range of what ceramic materials can typically withstand. Therefore, the cathode-supported design is more favorable than the separator-supported configuration not only from the electrical point of view, as it lowers the ohmic resistance in the separator drastically, but also from the mechanical stability.

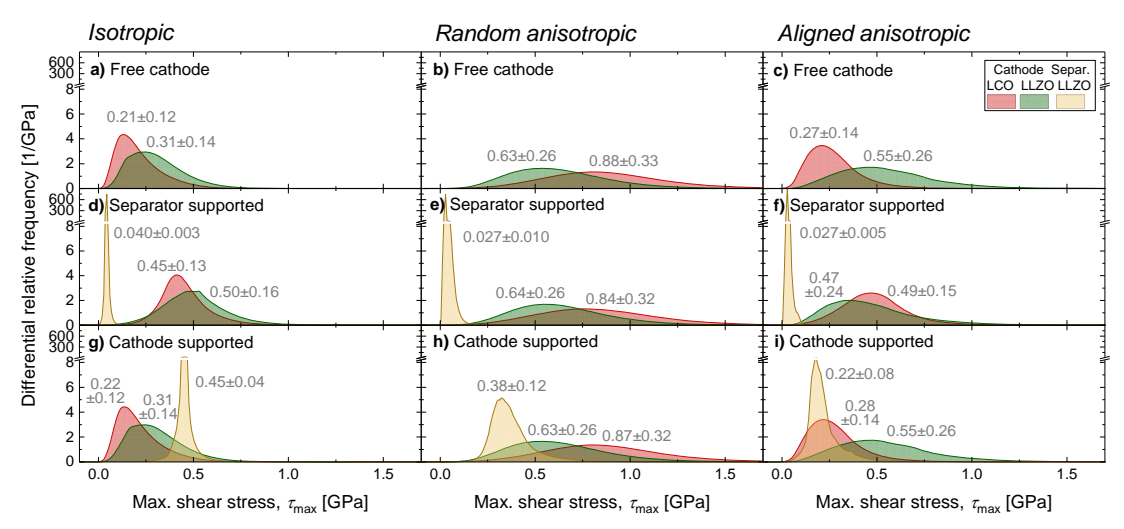


Fig. 5: Histograms of the maximal shear stress τ_{max} analogous to Fig. 4.

The maximum shear stresses $\tau_{\rm max}=(\sigma_1-\sigma_3)/2$ in Fig. 5 underline the previous statements. The results from the isotropic calculations underestimate the average and width of the stress distributions inside the mixed cathode (a,d,g) and overestimate the stresses inside the separator of the cathode supported design (g) when compared with the realistic random anisotropic case (b,e,h). The stresses inside the mixed cathode are considerably reduced in particular for the LCO if the LCO crystals are oriented in parallel in the textured case (c,f,i). Considering the macroscopic strains of the cathode electrode (Tab. 2), the isotropic calculations overestimate the dimension changes compared to the realistic random anisotropic case. The textured alignment results in larger out-of-plane strains; however, the thickness changes are still very small, which the battery housing will tolerate.

Tab. 2: Overview of strains and thickness changes of the cathode electrode during charging for the different configurations investigated.

0 · · · · · · · · · · · · · · · · · · ·				
	Lateral / thickness strain (thickness change)			
	Isotropic	Random anisotropic	Aligned anisotropic	
Free cathode	+0.46% / +0.46%	+0.31% / +0.31%	-0.19% / +1.61%	
Separator	+0.03% / +0.74% (0.37 μm)	+0.03% / +0.52% (0.26 μm)	-0.03% / +1.56% (0.78 μm)	
supported				
Cathode supported	+0.44% / +0.46% (0.46 μm)	+0.29% / +0.32% (0.32 μm)	-0.18% / +1.64% (1.6 μm)	

As stated before, all typical wet-chemical coating processes (roll-coating, screen-printing, tape casting, etc.) will induce a texture if the starting powder contains elongated non-spherical particles. The degree of alignment will primarily depend on the extent of this elongation. The more elongated the particles of the active material are in the crystallographic a and b direction compared to the c direction (as for the flake-like geometry used in this work), the more frequent they will be aligned horizontally in plane with the c axis pointing out of plane. Process parameters can also influence the degree of alignment: increasing the time of shearing during which the viscosity of the typically shear-thinning carrier liquid is lowered or increasing the shear rate of the coating process itself will amplify the texture. Using these experimental factors, the more favourable textured microstructure can be realised.

4. Conclusions

It is essential to consider the anisotropic properties of layered oxides when calculating the stress in composite cathodes of all-solid-state batteries. The anostropic expansion does not just effect individual particles, but is also crucial for the assessment of the average stresses in the mixed cathode, in particular when it is constrained (e.g. in an separator-supported cell design). This requires the following additional information compared to isotropic calculations: (1) The anisotropic expansions along the crystallographic axes. (2) The anisotropic stiffness matrix. (3) The crystallographic orientation of the active material grains inside the microstructure.

For our model system LCO/LLZO, the LLZO in the composite cathode suffers siginificant tensile stresses in all configurations which may lead to mechanical and electrochemical degradation and is seen as a possibly dominating factor of the decreasing cell performance. The stress orientation inside the LCO component agrees with its sheet-wise disintegration observed in experiment. The textured parallel alignment of the crystallographic *a-b* plane of the LCO along the coating plane leads to superior stress distribitions in all investigated configurations. It will result in more tolerable compressive stresses instead of tensile stresses in the separator and smaller stress values inside LCO. Remarkably, the cathode-supported cell configuration which leads to a smaller internal resistance of the cell, is also more favorable than the separator-supported configuration in terms of mechanical stability. This confirms the interest of using thin separators to optimise both electrical performance and mechanical stability.

Further work has to focus on minimising the stress in the microstructure itself. Possible approaches are to develop materials with lower intrinsic volume change, design a strain tolerant microstructure (by adapted pore geometry, use of segmentation or fibre network with infiltrated active material), mix expanding and shrinking active materials, or to include viscoelastic polymers inside the composite cathode. The methodology presented in this work can be used to assess also the stress state of those microstructures.

Acknowledgements

We thank Dr. K. Kelm, German Aerospace Center Cologne (Deutsches Zentrum für Luftund Raumfahrt, DLR), Institute of Material Research, for the acquisition of the FIB SEM image sequence and Dr. E. Wessel, Institute of Energy and Climate Research, IEK-2, Jülich for carrying out the EBSD analysis. Financial support from the German Federal Ministry of Education and Research (Bundesministerium für Bildung und Forschung), Projects Festbatt and CatSE, is thankfully acknowledged.

References

- [1] J. Janek and W. G. Zeier, A Solid Future for Battery Development, Nat Energy 1 (2016) 16141. https://doi.org/10.1038/NENERGY.2016.141.
- [2] M. Murayama, R. Kanno, M. Irie, S. Ito, T. Hata, N. Sonoyama, and Y. Kawamoto, Synthesis of New Lithium Ionic Conductor Thio-LISICON Lithium Silicon Sulfides System, J. Solid State Chem. 168[1] (2002) 140-48. https://doi.org/10.1006/jssc.2002.9701.
- [3] N. Kamaya, K. Homma, Y. Yamakawa, M. Hirayama, R. Kanno, M. Yonemura, T. Kamiyama, Y. Kato, S. Hama, K. Kawamoto, and A. Mitsui, A Lithium Superionic Conductor, Nat. Mater. 10[9] (2011) 682-86. https://doi.org/10.1038/Nmat3066.

- [4] R. Kanno and M. Maruyama, Lithium Ionic Conductor Thio-LISICON The Li₂S-GeS₂-P₂S₅ System, J. Electrochem. Soc. 148[7] (2001) A742-A46. https://doi.org/10.1149/1.1379028.
- [5] Y. G. Lee, S. Fujiki, C. Jung, N. Suzuki, N. Yashiro, R. Omoda, D. S. Ko, T. Shiratsuchi, T. Sugimoto, S. Ryu, J. H. Ku, T. Watanabe, Y. Park, Y. Aihara, D. Im, and I. T. Han, High-energy long-cycling all-solid-state lithium metal batteries enabled by silver-carbon composite anodes, Nat Energy 5[4] (2020) 299-308. https://doi.org/10.1038/s41560-020-0575-z.
- [6] L. J. Miara, W. D. Richards, Y. E. Wang, and G. Ceder, First-Principles Studies on Cation Dopants and Electrolyte Cathode Interphases for Lithium Garnets, Chem. Mater. 27[11] (2015) 4040-47. https://doi.org/10.1021/acs.chemmater.5b01023.
- [7] F. D. Han, Y. Z. Zhu, X. F. He, Y. F. Mo, and C. S. Wang, Electrochemical Stability of $\text{Li}_{10}\text{GeP}_2\text{S}_{12}$ and $\text{Li}_7\text{La}_3\text{Zr}_2\text{O}_{12}$ Solid Electrolytes, Adv Energy Mater 6[8] (2016) 1501590. https://doi.org/10.1002/aenm.201501590.
- [8] W. D. Richards, L. J. Miara, Y. Wang, J. C. Kim, and G. Ceder, Interface Stability in Solid-State Batteries, Chem. Mater. 28[1] (2016) 266-73. https://doi.org/10.1021/acs.chemmater.5b04082.
- [9] M. Finsterbusch, T. Danner, C. L. Tsai, S. Uhlenbruck, A. Latz, and O. Guillon, High Capacity Garnet-Based All-Solid-State Lithium Batteries: Fabrication and 3D-Microstructure Resolved Modeling, ACS Appl. Mater. Interfaces 10[26] (2018) 22329-39. https://doi.org/10.1021/acsami.8b06705.
- [10] C. L. Tsai, Q. L. Ma, C. Dellen, S. Lobe, F. Vondahlen, A. Windmuller, D. Gruner, H. Zheng, S. Uhlenbruck, M. Finsterbusch, F. Tietz, D. Fattakhova-Rohlfing, H. P. Buchkremer, and O. Guillon, A garnet structure-based all-solid-state Li battery without interface modification: resolving incompatibility issues on positive electrodes, Sustain Energ Fuels 3[1] (2019) 280-91. https://doi.org/10.1039/c8se00436f.
- [11] A. O. Kondrakov, A. Schmidt, J. Xu, H. Gesswein, R. Monig, P. Hartmann, H. Sommer, T. Brezesinski, and J. Janek, Anisotropic Lattice Strain and Mechanical Degradation of High- and Low-Nickel NCM Cathode Materials for Li-Ion Batteries, J. Phys. Chem. C 121[6] (2017) 3286-94. https://doi.org/10.1021/acs.jpcc.6b12885.
- [12] T. Li, X.-Z. Yuan, L. Zhang, D. Song, K. Shi, and C. Bock, Degradation Mechanisms and Mitigation Strategies of Nickel-Rich NMC-Based Lithium-Ion Batteries, Electrochemical Energy Reviews 3[1] (2020) 43-80. https://doi.org/10.1007/s41918-019-00053-3.
- [13] W. Hua, S. Wang, M. Knapp, S. J. Leake, A. Senyshyn, C. Richter, M. Yavuz, J. R. Binder, C. P. Grey, H. Ehrenberg, S. Indris, and B. Schwarz, Structural insights into the formation and voltage degradation of lithium- and manganese-rich layered oxides, Nature Communications 10[1] (2019) 5365. https://doi.org/10.1038/s41467-019-13240-z.
- [14] P. Teichert, G. G. Eshetu, H. Jahnke, and E. Figgemeier, Degradation and Aging Routes of Ni-Rich Cathode Based Li-Ion Batteries, Batteries 6[1] (2020) 8. https://www.mdpi.com/2313-0105/6/1/8.
- [15] L. de Biasi, A. O. Kondrakov, H. Gesswein, T. Brezesinski, P. Hartmann, and J. Janek, Between Scylla and Charybdis: Balancing Among Structural Stability and Energy Density of Layered NCM Cathode Materials for Advanced Lithium-Ion Batteries, J. Phys. Chem. C 121[47] (2017) 26163-71. https://doi.org/10.1021/acs.jpcc.7b06363.

- [16] J. P. Pender, G. Jha, D. H. Youn, J. M. Ziegler, I. Andoni, E. J. Choi, A. Heller, B. S. Dunn, P. S. Weiss, R. M. Penner, and C. B. Mullins, Electrode Degradation in Lithium-Ion Batteries, ACS Nano 14[2] (2020) 1243-95. https://doi.org/10.1021/acsnano.9b04365.
- [17] L. Mu, R. Lin, R. Xu, L. Han, S. Xia, D. Sokaras, J. D. Steiner, T.-C. Weng, D. Nordlund, M. M. Doeff, Y. Liu, K. Zhao, H. L. Xin, and F. Lin, Oxygen Release Induced Chemomechanical Breakdown of Layered Cathode Materials, Nano Lett. 18[5] (2018) 3241-49. https://doi.org/10.1021/acs.nanolett.8b01036.
- [18] A. Mukhopadhyay and B. W. Sheldon, Deformation and stress in electrode materials for Li-ion batteries, Progress in Materials Science 63 (2014) 58-116. https://doi.org/10.1016/j.pmatsci.2014.02.001.
- [19] Y. He, C. Lu, S. Liu, W. Zheng, and J. Luo, Interfacial Incompatibility and Internal Stresses in All-Solid-State Lithium Ion Batteries, Adv Energy Mater 9[36] (2019) 1901810. https://doi.org/10.1002/aenm.201901810.
- [20] P. Li, Y. B. Zhao, Y. X. Shen, and S. H. Bo, Fracture behavior in battery materials, J Phys-Energy 2[2] (2020). https://doi.org/10.1088/2515-7655/ab83e1.
- [21] T. Ohzuku and A. Ueda, Solid-State Redox Reactions of LiCoO₂ (R3m) for 4 Volt Secondary Lithium Cells, J. Electrochem. Soc. 141[11] (1994) 2972-77. https://doi.org/10.1149/1.2059267.
- [22] J. N. Reimers and J. R. Dahn, Electrochemical and In Situ X-Ray Diffraction Studies of Lithium Intercalation in Li_xCoO₂, J. Electrochem. Soc. 139[8] (1992) 2091-97. https://doi.org/10.1149/1.2221184.
- [23] R. Koerver, W. Zhang, L. de Biasi, S. Schweidler, A. O. Kondrakov, S. Kolling, T. Brezesinski, P. Hartmann, W. G. Zeier, and J. Janek, Chemo-mechanical expansion of lithium electrode materials on the route to mechanically optimized all-solid-state batteries, Energ Environ Sci 11[8] (2018) 2142-58. https://doi.org/10.1039/C8EE00907D.
- [24] S. A. Roberts, V. E. Brunini, K. N. Long, and A. M. Grillet, A Framework for Three-Dimensional Mesoscale Modeling of Anisotropic Swelling and Mechanical Deformation in Lithium-Ion Electrodes, J. Electrochem. Soc. 161[11] (2014) F3052-F59. https://doi.org/10.1149/2.0081411jes.
- [25] C. Lim, B. Yan, L. L. Yin, and L. K. Zhu, Simulation of diffusion-induced stress using reconstructed electrodes particle structures generated by micro/nano-CT, Electrochim. Acta 75 (2012) 279-87. https://doi.org/10.1016/j.electacta.2012.04.120.
- [26] J. H. Seo, M. Chung, M. Park, S. W. Han, X. C. Zhang, and A. M. Sastry, Generation of Realistic Particle Structures and Simulations of Internal Stress: A Numerical/AFM Study of LiMn₂O₄ Particles, J. Electrochem. Soc. 158[4] (2011) A434-A42. https://doi.org/10.1149/1.3552930.
- [27] W. Mai, M. Yang, and S. Soghrati, A particle-resolved 3D finite element model to study the effect of cathode microstructure on the behavior of lithium ion batteries, Electrochim. Acta 294 (2019) 192-209. https://doi.org/10.1016/j.electacta.2018.10.072.
- [28] V. Malave, J. R. Berger, H. Y. Zhu, and R. J. Kee, A Computational Model of the Mechanical Behavior within Reconstructed Li_xCoO₂ Li-ion Battery Cathode Particles, Electrochim. Acta 130 (2014) 707-17. https://doi.org/10.1016/j.electacta.2014.03.113.
- [29] S. Yamakawa, N. Nagasako, H. Yamasaki, T. Koyama, and R. Asahi, Phase-field modeling of stress generation in polycrystalline LiCoO₂, Solid State Ionics 319 (2018) 209-17. https://doi.org/10.1016/j.ssi.2018.02.013.

- [30] U.-H. Kim, H.-H. Ryu, J.-H. Kim, R. Mücke, P. Kaghazchi, C. S. Yoon, and Y.-K. Sun, Microstructure-Controlled Ni-Rich Cathode Material by Microscale Compositional Partition for Next-Generation Electric Vehicles, Adv Energy Mater 0[0] (2019) 1803902. https://doi.org/10.1002/aenm.201803902.
- [31] H. H. Ryu, N. Y. Park, J. H. Seo, Y. S. Yu, M. Sharma, R. Mücke, P. Kaghazchi, C. S. Yoon, and Y. K. Sun, A highly stabilized Ni-rich NCA cathode for high-energy lithium-ion batteries, Materials Today 36 (2020) 73-82. https://doi.org/10.1016/j.mattod.2020.01.019.
- [32] R. E. Garcia, Y. M. Chiang, W. C. Carter, P. Limthongkul, and C. M. Bishop, Microstructural modeling and design of rechargeable lithium-ion batteries, J. Electrochem. Soc. 152[1] (2005) A255-A63. https://doi.org/10.1149/1.1836132.
- [33] L. Wu, Y. Wen, and J. Zhang, Three-Dimensional Finite Element Study on Li Diffusion Induced Stress in FIB-SEM Reconstructed LiCoO₂ Half Cell, Electrochim. Acta 222 (2016) 814-20. https://doi.org/10.1016/j.electacta.2016.11.042.
- [34] L. Wu, X. Xiao, Y. Wen, and J. Zhang, Three-dimensional finite element study on stress generation in synchrotron X-ray tomography reconstructed nickel-manganese-cobalt based half cell, J. Power Sources 336 (2016) 8-18. https://doi.org/10.1016/j.jpowsour.2016.10.052.
- [35] H. Mendoza, S. A. Roberts, V. E. Brunini, and A. M. Grillet, Mechanical and Electrochemical Response of a LiCoO₂ Cathode using Reconstructed Microstructures, Electrochim. Acta 190 (2016) 1-15. https://doi.org/10.1016/j.electacta.2015.12.224.
- [36] E. J. Cheng, N. J. Taylor, J. Wolfenstine, and J. Sakamoto, Elastic properties of lithium cobalt oxide (LiCoO₂), Journal of Asian Ceramic Societies 5[2] (2017) 113-17. https://doi.org/10.1016/j.jascer.2017.03.001.
- [37] A. A. Hubaud, D. J. Schroeder, B. J. Ingram, J. S. Okasinski, and J. T. Vaughey, Thermal expansion in the garnet-type solid electrolyte (Li_{7-x}Al_{x/3})La₃Zr₂O₁₂ as a function of Al content, J. Alloys Compd. 644 (2015) 804-07. https://doi.org/10.1016/j.jallcom.2015.05.067.
- [38] S. Baker and I. Matthews, Lucas-Kanade 20 years on: A unifying framework, International Journal of Computer Vision 56[3] (2004) 221-55. https://doi.org/DOI 10.1023/B:VISI.0000011205.11775.fd.
- [39] M. J. Black, G. Sapiro, D. H. Marimont, and D. Heeger, Robust anisotropic diffusion, Ieee Transactions on Image Processing 7[3] (1998) 421-32. https://doi.org/10.1109/83.661192.
- [40] X. Wang, I. Loa, K. Kune, K. Syassen, and M. Amboage, Effect of pressure on the structural properties and Raman modes of LiCoO₂, Phys Rev B 72[22] (2005). https://doi.org/10.1103/PhysRevB.72.224102.
- [41] Y. Takahashi, N. Kijima, K. Dokko, M. Nishizawa, I. Uchida, and J. Akimoto, Structure and electron density analysis of electrochemically and chemically delithiated LiCoO₂ single crystals, J. Solid State Chem. 180[1] (2007) 313-21. https://doi.org/10.1016/j.jssc.2006.10.018.
- [42] M. Qu, W. H. Woodford, J. M. Maloney, W. C. Carter, Y. M. Chiang, and K. J. Van Vliet, Nanomechanical Quantification of Elastic, Plastic, and Fracture Properties of LiCoO₂, Adv Energy Mater 2[8] (2012) 940-44. https://doi.org/10.1002/aenm.201200107.

- [43] L. M. Wu and J. Zhang, Ab initio study of anisotropic mechanical properties of LiCoO₂ during lithium intercalation and deintercalation process, J. Appl. Phys. 118[22] (2015). https://doi.org/10.1063/1.4937409.
- [44] O. L. Anderson, A simplified method for calculating the debye temperature from elastic constants, J. Phys. Chem. Solids 24[7] (1963) 909-17. https://doi.org/10.1016/0022-3697(63)90067-2.
- [45] A. N. Wang, J. F. Nonemacher, G. Yan, M. Finsterbusch, J. Malzbender, and M. Kruger, Mechanical properties of the solid electrolyte Al-substituted Li₇La₃Zr₂O₁₂ (LLZO) by utilizing micro-pillar indentation splitting test, J. Eur. Ceram. Soc. 38[9] (2018) 3201-09. https://doi.org/10.1016/j.jeurceramsoc.2018.02.032.
- [46] J. E. Ni, E. D. Case, J. S. Sakamoto, E. Rangasamy, and J. B. Wolfenstine, Room temperature elastic moduli and Vickers hardness of hot-pressed LLZO cubic garnet, J. Mater. Sci. 47[23] (2012) 7978-85. https://doi.org/10.1007/s10853-012-6687-5.
- [47] S. Yu, R. D. Schmidt, R. Garcia-Mendez, E. Herbert, N. J. Dudney, J. B. Wolfenstine, J. Sakamoto, and D. J. Siegel, Elastic Properties of the Solid Electrolyte Li₇La₃Zr₂O₁₂ (LLZO), Chem. Mater. 28[1] (2016) 197-206. https://doi.org/10.1021/acs.chemmater.5b03854.
- [48] H. F. Wang, Y. I. Jang, B. Y. Huang, D. R. Sadoway, and Y. T. Chiang, TEM study of electrochemical cycling-induced damage and disorder in LiCoO₂ cathodes for rechargeable lithium batteries, J. Electrochem. Soc. 146[2] (1999) 473-80. https://doi.org/Doi 10.1149/1.1391631.
- [49] L. Feng, X. F. Lu, T. T. Zhao, and S. Dillon, The effect of electrochemical cycling on the strength of LiCoO₂, J. Am. Ceram. Soc. 102[1] (2019) 372-81. https://doi.org/10.1111/jace.15893.
- [50] G. Yan, J. F. Nonemacher, H. Zheng, M. Finsterbusch, J. Malzbender, and M. Kruger, An investigation on strength distribution, subcritical crack growth and lifetime of the lithium-ion conductor Li₇La₃Zr₂O₁₂, J. Mater. Sci. 54[7] (2019) 5671-81. https://doi.org/10.1007/s10853-018-03251-4.
- [51] H.-Y. Li, Enhanced mechanical strength and ionic conductivity of LLZO solid electrolytes by oscillatory pressure sintering, Ceram. Int. 45[14] (2019) 18115-18.